Check for updates

Silver nanoparticles-decorated NiFe$_2$O$_4$/polyaniline ternary nanocomposite for electromagnetic interference shielding

Monika Saini[1] · Rajni Shukla[1]

Abstract

In this study, silver nanoparticle-embedded NiFe$_2$O$_4$/polyaniline ternary nanocomposites were prepared via chemical in situ polymerization. The synthesized nanocomposites were fully characterized by X-ray diffraction (XRD), Fourier transform infrared spectroscopy (FTIR), high-resolution transmission electron microscopy (HR-TEM), four-probe resistivity (FPR), vibrating sample magnetometer (VSM), thermal gravimetric analysis (TGA), and vector network analyzer (VNA). XRD, FTIR, and HR-TEM analyses showed comprehensive structural and morphological evidences for as-prepared ternary compositions with varying particle size (~ 45 to 60 nm). The electrical conductivity of nanocomposites was significantly affected by the mixing of silver nanoparticles in FPR results. VSM study revealed that the prepared nanocomposites exhibit ferromagnetism at room temperature due to existence of ferrite nanoparticles. TGA indicated the enhanced thermal stability of the resulting products with increasing ratio of ferrite and silver contents. VNA study demonstrated the remarkable shielding performance (SE ~ 35.17 dB) of obtained samples with a sample thickness of 2.0 mm in the frequency range of 8.2–12.4 GHz, which is mainly attributed to the synergistic effect of polyaniline, nickel ferrite, and silver particles. These results indicated that these composite materials with ideal electromagnetic properties are best suited for EMI shielding applications.

1 Introduction

In the modern world, the rapid development of electronics technology has resulted in a new type of pollution known as electromagnetic (EM) pollution or electromagnetic interference (EMI) [1, 2]. EMI not only affects the usual functions of electronic or electrical gadgets but also has adverse effects on living beings [3]. Therefore, to solve EMI problem, high-performance shielding materials are in worldwide demand. An ideal shielding material should be lightweight, corrosion-resistant, economically feasible, and environmentally stable [4, 5].

In the last few years, conducting polymers (CPs) have been extensively studied due to their numerous applications in various technological fields [6, 7]. Among these conductive polymers, polyaniline (PANI) is the most investigated one because of its excellent conductivity, good environmental stability, ease of synthesis, flexibility, and its wide applications in lightweight batteries, supercapacitors,

anticorrosion coatings, OLEDs, EMI shielding, and electrochromic display devices [8–10].

Nowadays, much attention has been paid globally to the development of organic–inorganic hybrid materials. These nanostructured composites offer the synergic properties of both organic and inorganic materials, which are useful in various applications like cell separations, chemical sensors, drug delivery systems, electrochemical actuators, and stealth technology [11, 12].

Over the past decades, the spinel ferrites (general formula MFe$_2$O$_4$, where M is a divalent metal ion, e.g., Mg, Cu, Ni, Cd, etc.) have attracted significantly interest of scientists and researchers due to their potential applications such as magnetic recording devices, chokes, ferrofluids, microwave devices, transformer cores, and sensors [13, 14]. They possess unique properties like high-saturation magnetization, large magnetocrystalline anisotropy, and high thermal and chemical resistance [14, 15]. In nanocrystalline ferrites, nickel ferrite (NiFe$_2$O$_4$) with inverse spinel ferrite structure is a well-known soft magnetic material with interesting features like high magnetic saturation, coercivity, and chemical stability. The position of the divalent cations (Ni^{2+}) in the crystal structure of nickel ferrite significantly affects its magnetic properties. So far, many applications of nickel ferrite have been reported in

✉ Rajni Shukla
  rajnishukla3871@gmail.com

[1] Department of Physics, Deenbandhu Chottu Ram University of Science & Technology, Murthal, Sonepat, Haryana, India

various domains such as gas-sensing, high-frequency devices, magnetic fluids, printing, magnetic refrigerators, and catalysts [16–18].

From the study of previously reported results, it has been observed that several researchers have fabricated conductive/ferrite materials with interesting electromagnetic properties owing to synergistic contributions from the conductive matrix and ferrite fillers. Yavuz et al. reported the fabrication and properties of MnZn and NiMnZn ferrite–polyaniline nanocomposite [19]. Madhu et al. synthesized polyaniline/$Ni_{0.5}Zn_{0.5}Fe_2O_4$ composites with maximum electromagnetic shielding value of 55.14 dB at 50 Hz [20]. Wang et al. studied the microwave absorption properties with a reflection loss < − 10 dB up to 5 GHz of $Ni_{0.5}Zn_{0.5}Fe_2O_4$/polyaniline nanocomposite [21]. Fabrication of conductive and magnetic $NiFe_{1.95}Gd_{0.05}O_4$ nanoparticles coated with polyaniline was reported by Aphesteguy et al. [22]. Wang et al. observed a minimum reflection loss of − 19.7 dB (− 21.5 dB) for polyaniline/polypyrrole-$BaFe_{12}O_{19}$/$Ni_{0.8}Zn_{0.2}Fe_2O_4$ composites at the frequency of 7.3 GHz (10.7 GHz) [23]. To the best of our knowledge, however, very few works based on metallic particle-decorated magnetic-conducting composites have been reported so far.

The shielding effectiveness of a material depends upon fine-tuning between its conductive and magnetic properties and also should possess characteristics such as diminutive size, eco-friendly, corrosion durability, low production cost, and wide frequency range.

Herein, the addition of metallic silver particles in the polymer matrix seems to be very interesting as it considerably enhances the thermal and electrical conductivity. It also improves the mechanical strength of the fabricated compound and offers different applications in electrical and electronic devices. This kind of ternary composites can be very beneficial for designing effective shielding material for commercial applications. So, the inclusion of silver nanoparticles in nickel ferrite/polyaniline can be tailored to acquire the unique mechanical properties in addition to significant electrical, magnetic, and thermal properties. As hybrid materials are preferred for various applications, the results of incorporation of conducting (silver) and magnetic (nickel ferrite) in conducting polymer (polyaniline) matrix need to be studied.

In this report, the structural, thermal, magnetic, and shielding properties of silver particles-decorated nickel ferrite/polyaniline nanocomposites prepared via chemical in situ polymerization have been investigated.

2 Experimental procedure

2.1 Chemicals and reagents

Aniline monomer and sodium dodecylbenzene sulfonate (DBSA) were purchased from Sigma Aldrich. The materials were synthesized using ammonium persulfate [$(NH_4)_2S_2O_8$], sodium borohydride ($NaBH_4$), ferric nitrate ($FeN_3O_9 \cdot 9H_2O$), nickel nitrate ($NiN_2O_6 \cdot 6H_2O$), silver nitrate ($AgNO_3$), oleic acid, and liquid ammonia of Loba Chemie and used as received. Aniline was purified before use.

2.2 Preparation of nanocrystalline $NiFe_2O_4$

Nickel ferrite (NF) was prepared by the chemical co-precipitation method using nickel nitrate and ferrite nitrate as starting materials. An equimolar amount of all materials was dissolved in distilled water and ultrasonicated for 1–2 h. After that surfactant oleic acid was added in the homogenous solution. Then, precipitating agent (liquid ammonia) was added slowly in the prepared solution by maintaining the pH value at 8–9. The final product was centrifuged to remove the impurities and sintered at 400 °C for 2 h.

### 2.3 Development of Ag-$NiFe_2O_4$@PANI ternary nanocomposite

PANI/$NiFe_2O_4$ nanocomposite was synthesized using the in situ oxidative polymerization of aniline with oxidant APS and surfactant DBSA (Fig. 1). The pre-synthesized $NiFe_2O_4$ particles were fully immersed in 0.3 M aqueous surfactant solution of DBSA. Subsequently, 0.1 M aniline was dissolved in reaction mixture and ultrasonicated for 3–4 h. Further, there was dropwise addition of 0.1 M APS oxidant solution at low temperature (0–10 °C) with uninterrupted stirring for 6–7 h. The prepared mixture was centrifuged with distilled water and isopropanol to remove extra additives and dried in the oven at 70 °C for 12 h.

For silver doping, a stoichiometric quantity of silver nitrate was added into 0.10 ml of the aqueous solution of PANI/$NiFe_2O_4$ nanocomposite and vigorously stirred for 30 min. For the reduction process, an aqueous solution of sodium borohydride was added dropwise to the above mixture under steady stirring at 95 °C. The prepared mixture was washed and dried at 65 °C. Nanocomposites with different weight percentage ratios of silver particles (0.25, 0.5, and 0.75) were fabricated and designated as ANP1, ANP2, and ANP3, respectively.

2.4 Physical characterization

The crystalline and structural parameters of developed nanocomposites were determined through X-ray diffractometer

Fig. 1 Diagrammatic representation of preparation of Ag/NiFe2O4/PANI nanocomposite

3 Results and discussion

3.1 Structural confirmation
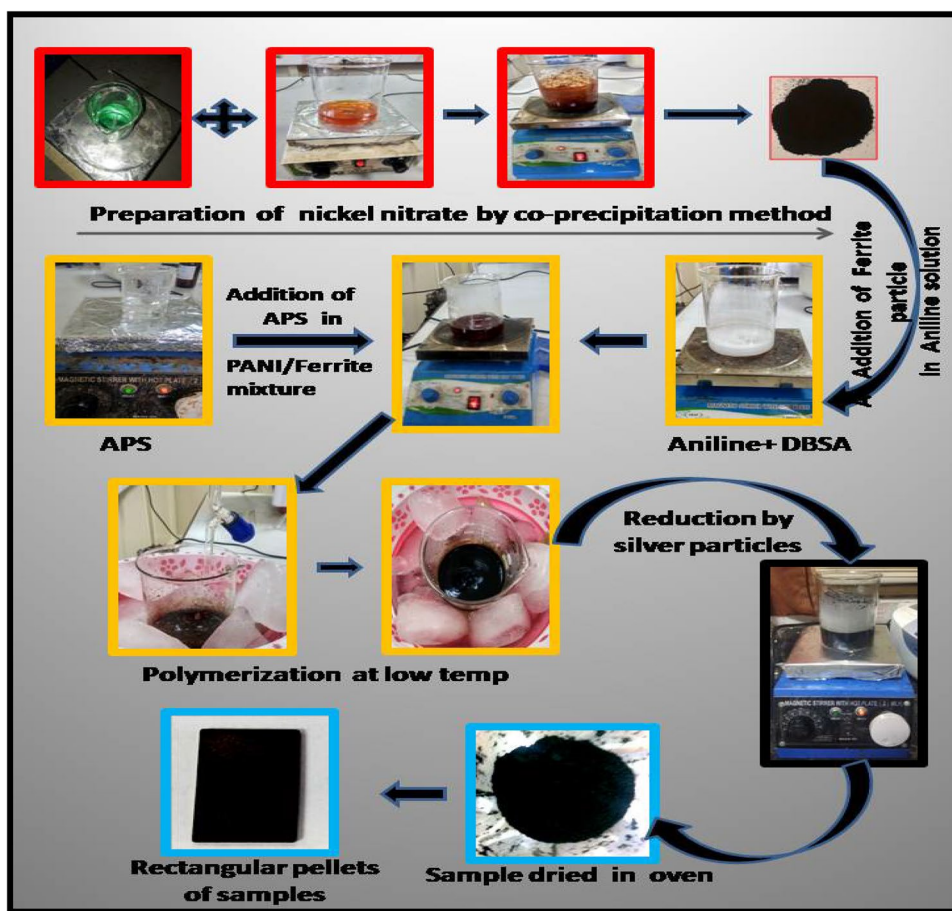
(Rigaku IV, Japan) using CuKα radiation in the scattered angle range of $2\theta = 10$–$70°$ at room temperature. Microstructure images of samples were obtained through HR-TEM (Model Technai G2). FTIR spectral analysis was carried out on Perkin–Elmer Frontier spectrometer, with a wave number range of 400–4000 cm^{-1}. Conductive properties (DC) of the as-grown products were investigated through the four-probe device (Keithley 4200 source meter). VSM (Lakeshore, USA) technique was employed to examine the magnetic properties at maximum applied magnetic field of $\pm$ 10 kOe. To study the thermal stability of materials, TGA was performed on Perkin Elmer STA 6000 from room temperature to 700 °C in nitrogen ambient at a heat pace of 10 °C/min. Further, EMI shielding parameters were measured by VNA instrument (Model N5230C) with rectangular pellet shape samples (thickness ~ 2.0 mm) using a copper waveguide in the X-band frequency regime.

XRD profile of PANI, $NiFe_2O_4$, ANP1, ANP2, and ANP3 materials is shown in Fig. 2. XRD spectra of pristine PANI exhibit two characteristic peaks at $2\theta = 20.79°$ ($d = 4.712$ Å) and $25.08°$ ($d = 3.568$ Å), which represents the polycrystalline nature of PANI due to parallel and perpendicular periodicity of atoms in polyaniline chain, respectively [24]. These peaks' intensity become diminished in composites, indicating that PANI had transformed into a completely amorphous state due to the interaction between the polymer chain, silver, and ferrite nanoparticles. The recorded X-ray pattern of $NiFe_2O_4$ shows the presence of strong diffraction peaks at $2\theta = 30.64°$,
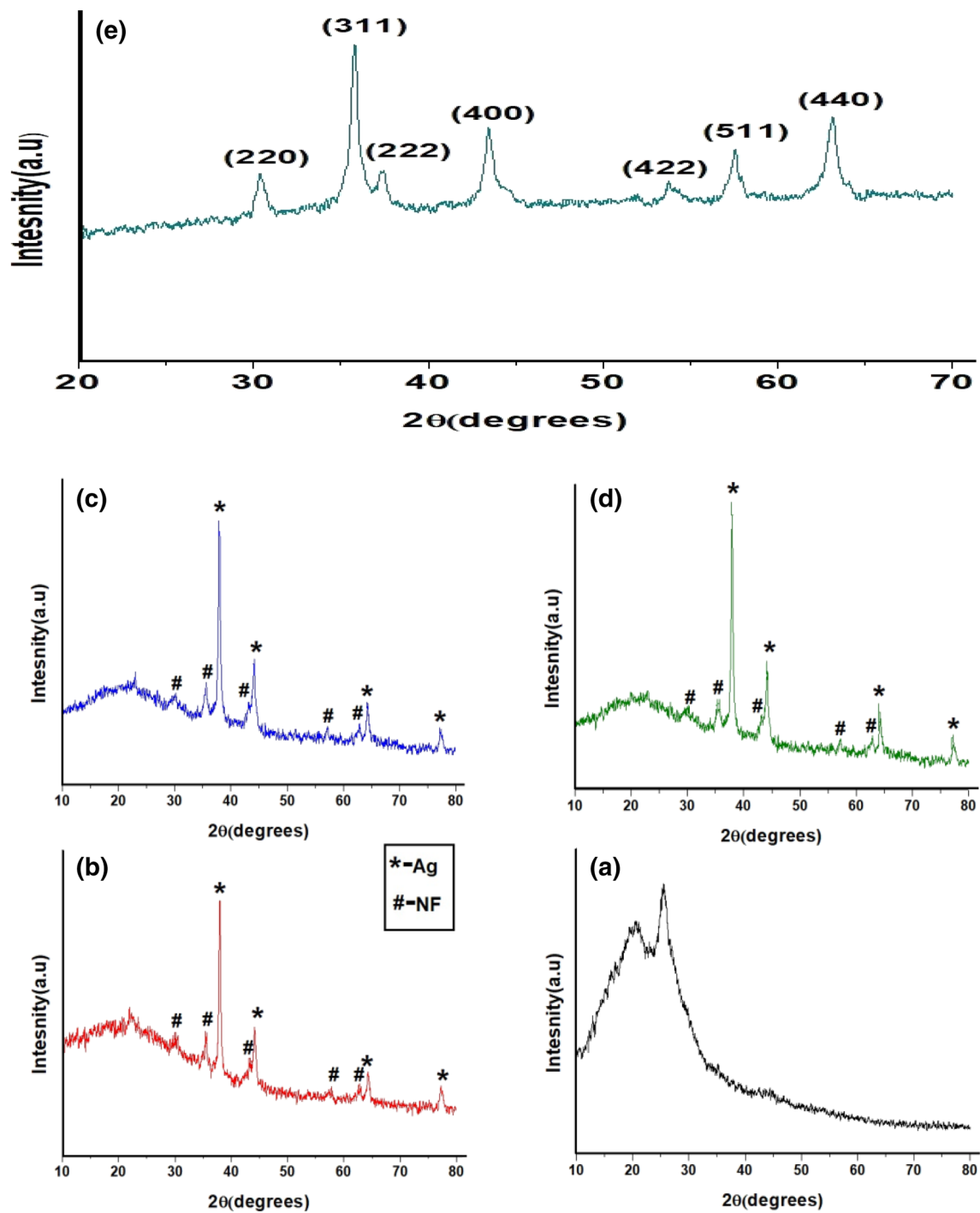
Fig. 2 XRD spectra of **a** PANI, **b** ANP1, **c** ANP2, **d** ANP3, and **e** pure NF

35.57°, 38.12°, 43.58°, 57.29°, and 62.73° corresponds to (220), (311), (222), (400), (511), and (440) reflection planes, respectively (JCPDS no. 10-0325), confirming the spinel cubic structure of material. These peaks are well matched with reported results [25, 26]. No extra phases of impurities were detected in synthesized samples, revealing their high purity. The well-resolved peaks at 2θ of 38.51°, 44.46°, 64.59°, and 77.51° are ascribed to the crystal planes (111), (200), (220), and (311) of silver particles with cubic symmetry (JCPDS no. 04-0783). As one can see, XRD images of ternary nanocomposites exhibit all the main phases of silver and ferrite materials. However, their intensity decreases due to encapsulation by polyaniline, which suppressed the crystalline behavior of ferrite

and silver particles. The existence of all reflection peaks of $NiFe_2O_4$, Ag, and PANI in the diffraction pattern of nanocomposites demonstrates the successful synthesis of ANP ternary nanocomposites.

The calculated crystallite sizes (D) of synthesized samples were estimated from the most intense (311) reflection peak through the following Debye–Scherrer formula [27].

$$D = \frac{0.89\lambda}{\beta \cos\theta} \quad (1)$$

where β is the full-width at half-maximum intensity (FWHM), λ is the wavelength of X-ray source ($\lambda = 0.154051$ nm), and θ is Bragg diffraction angle.

The lattice parameter (a) corresponding to miller indices [311] is determined via below relation [28]:

$$a = d\sqrt{h^2 + k^2 + l^2} \quad (2)$$

where d is the inter-plane spacing.

The distance between magnetic ions at tetrahedral [A] and octahedral [B] sites is obtained using the formula [29]:

$$L_A = \frac{a\sqrt{3}}{4} \quad (3)$$

and

$$L_B = \frac{a\sqrt{2}}{4} \quad (4)$$

The evaluated crystallite size of nickel ferrite and nanocomposites ANP1, ANP2, and ANP3 is found to be 11.67, 18.89, 28.27, and 35.43 nm, respectively, in increasing order due to increase in grain growth of particles as a result of increasing interaction of PANI, ferrite, and silver particles. The calculated structural parameters are listed in Table 1. The XRD results authenticated the crystalline structure of ternary nanocomposites is similar to that of NF, which is a cubical spinel ferrite, crystallizing in the cubical spinel geometry ($a = 0.8356$ nm), space group Fd3 m. Assuming the atomic occupancy, $NiFe_2O_4$ is described in terms of cationic distribution as $(Fe^{3+})_A [Ni^{2+} Fe^{3+}]_B O_4^{2-}$ [30, 31]. The reduction in lattice parameter might have caused by lattice

disorder in ferrite nanostructures due to the incorporation of polymer contents, which reduce crystal component due to changing electrostatic interaction between ferrite particles.

3.2 TEM study

Figure 3 shows the microstructure images of the $NiFe_2O_4$ and $Ag/NiFe_2O_4/PANI$ composite materials obtained by TEM analysis. The TEM image of nickel ferrite reveals that mostly nanoparticles are spherical in shape with little agglomeration between them (Fig. 3a), which is in agreement with the reported results.[32]. In Fig. 3c of Ag/$NiFe_2O_4/PANI$ nanocomposite, the dark particles are attributed to $Ag/NiFe_2O_4$, while the gray part is representing the polyaniline. $NiFe_2O_4$ and Ag nanoparticles are agglomerated attached to the PANI surface because of the interactions between magnetic dipole of $NiFe_2O_4$ and polyaniline. The average particle sizes of these nanocomposites were estimated in the range of 45–60 nm as shown in the histogram image (Fig. 3f), which is consistent with the XRD results. The SAED pattern depicts the crystalline nature of fabricated nanocomposite (Fig. 3d). The EDX analysis (Fig. 3g) confirmed the existence of all principal elemental composition C, O, N, Ni, Fe, and Ag in the synthesized ternary samples. Hence, TEM analysis also verified the successful fabrication of ANP nanocomposites.

3.3 FTIR analysis

The FTIR characteristics peaks (Fig. 4) of PANI occur at 1547, 1498, 1297, 1182, 1036, and 854 cm^{-1}, which is consistent with reported results [33]. The major peaks at 1547 and 1498 cm^{-1} is assigned to the C=N and C=C stretching mode of vibration of quinone and benzenoid units in polyaniline structure. The adsorption band at around 1297 cm^{-1} is associated with C–N stretching deformation with aromatic conjugation. The band assigned at 1182 cm^{-1} is ascribed to C–H bending in plane for 1, 4-disubstituted benzene ring. The peak located at 1036 cm^{-1} is attributed to the –SO_3H group. The peak observed at 1640 cm^{-1} arises due to the creation of the carbonyl group owing to excess oxidation of the alkyl chain group of dodecylbenzene sulfonic acid. The peak at 854 cm^{-1} is caused by aromatic C–C out of plane bending for benzenoid unit [34, 35]. Another widespread band at 3431 cm^{-1} is corresponding to the N–H stretching vibration of aromatic amines. In the FTIR spectrum of ANP nanocomposites, the presence of characteristics bands at 586 cm^{-1} and 475 cm^{-1} are due to tetrahedral and octahedral vibrational modes of ferrite, respectively [36]. Further, in the case of the nanocomposites, the intensity of benzenoid and quinoid peaks is higher in comparison of pure polyaniline, which reveals the embedment of silver

Table 1 Measured structural parameters of NF and ANP1, ANP2, and ANP3 composites at the sharpest peak (311)

Sample	Lattice constant (Å)	Crystallite size (nm)	L_A (Å)	L_B (Å)
NF	8.356	11.67	3.59	2.92
ANP1	8.228	18.89	3.53	2.88
ANP2	8.179	28.27	3.51	2.86
ANP3	8.012	35.43	3.46	2.83

Fig. 3 TEM images of **a** NF, **c** and **e** ANP3 nanocomposite, **b** SAED pattern of NF, **d** SAED pattern of ANP3 composite **f** Histogram of the particle size distribution, and **g** EDAX map of ANP3 nanocomposite
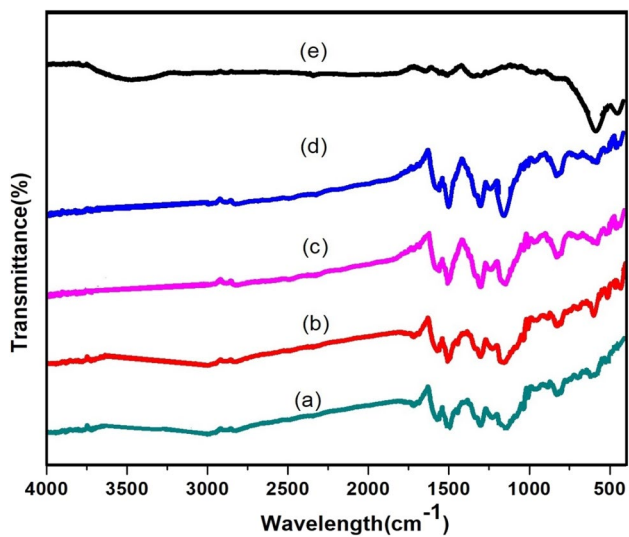
g
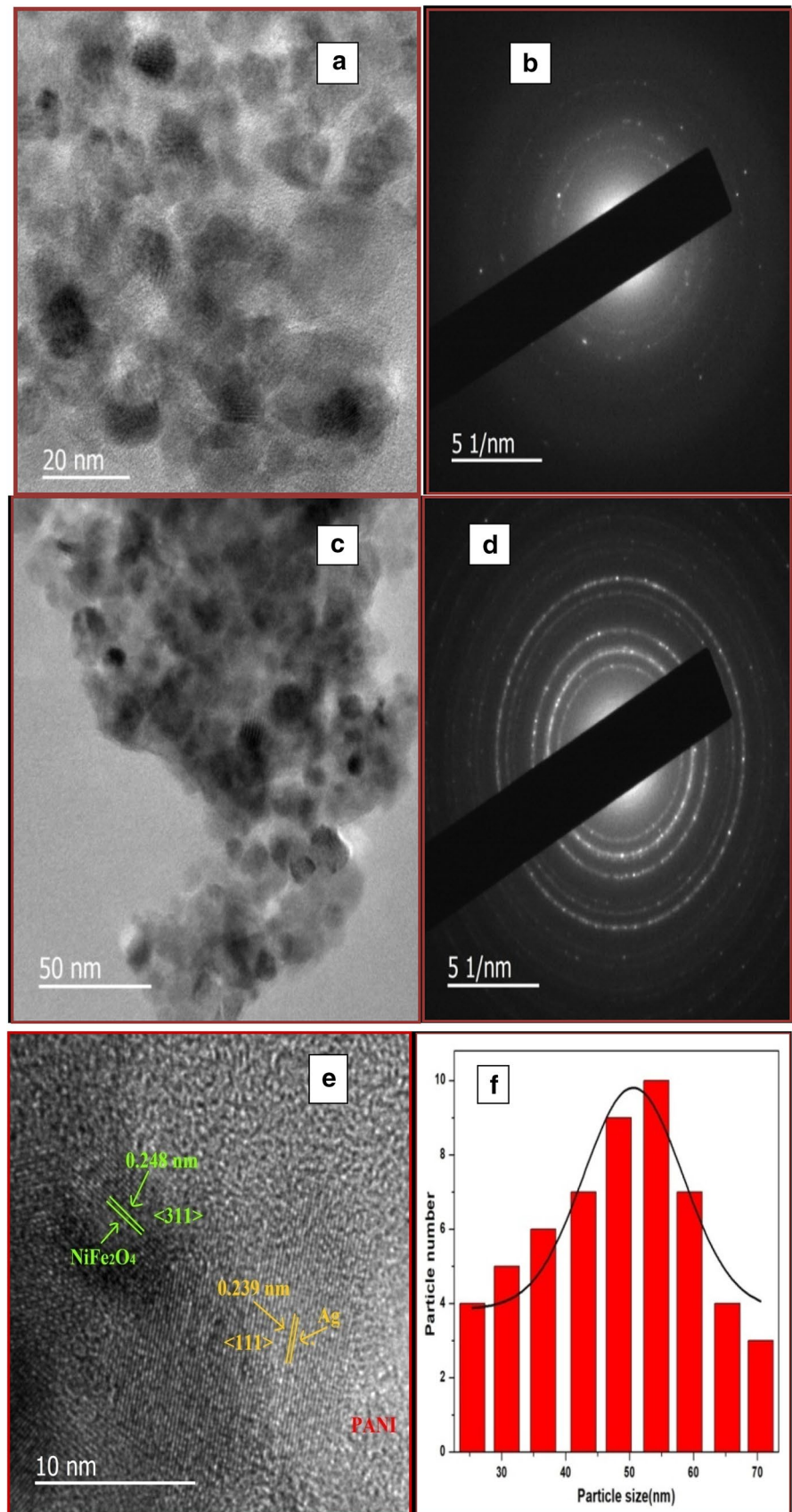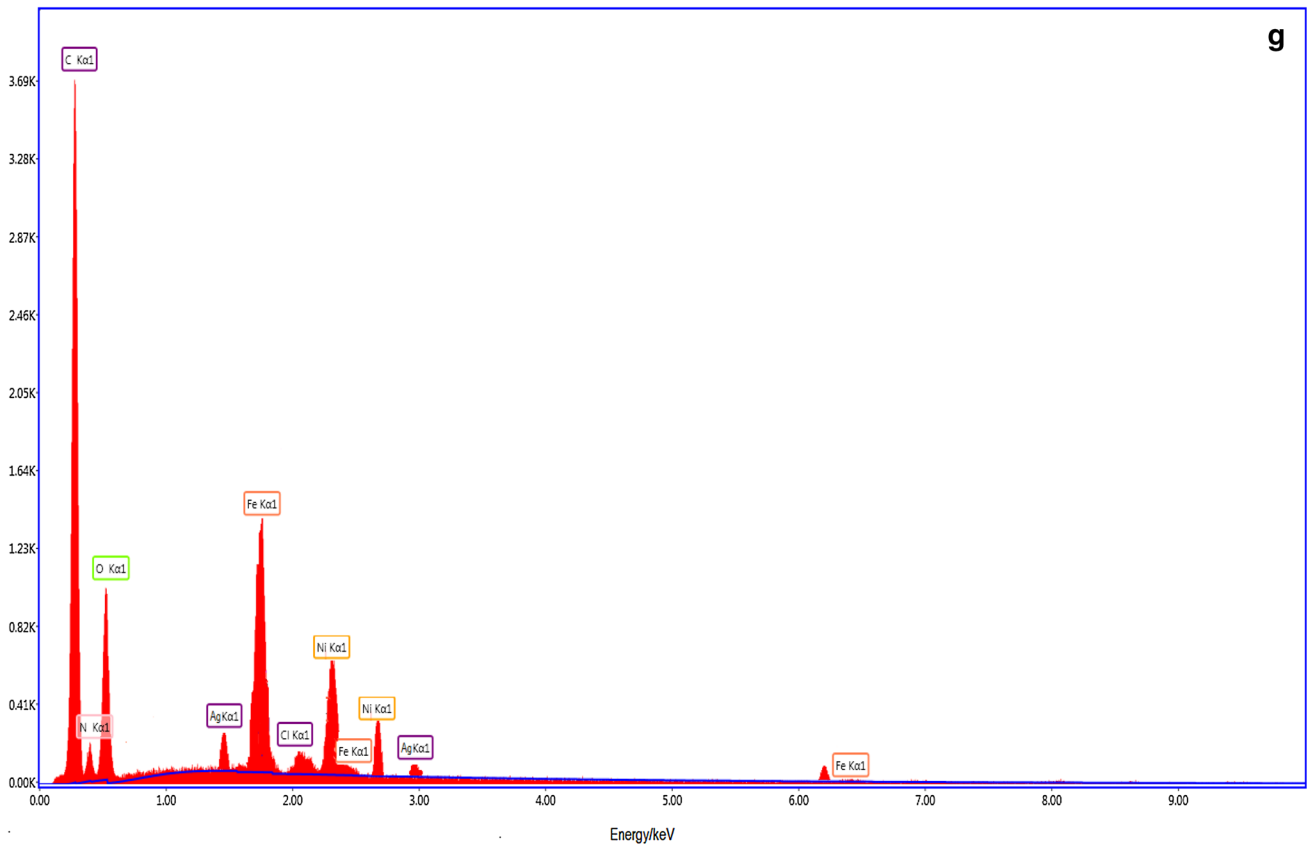
Fig. 3 (continued)

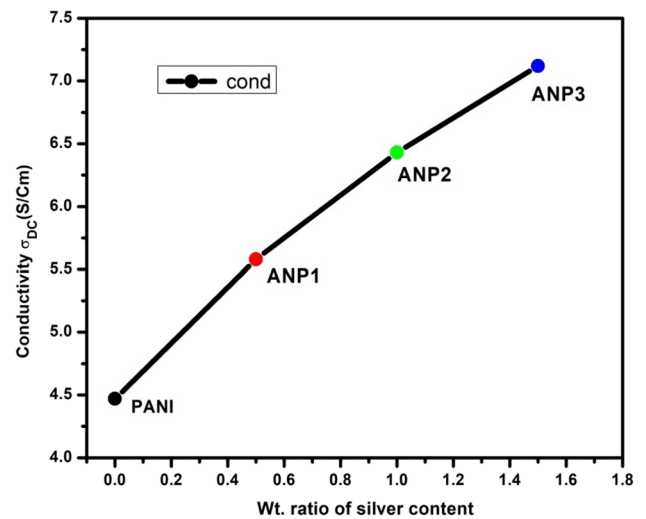**Fig. 4** FTIR spectrum of **a** PANI, **b** ANP1, **c** ANP2, **d** ANP3, and **e** pure NF

Fig. 5 Variation of conductivity (DC) of PANI and ANP composites with varying concentration of silver particles

particles in conducting/magnetic nanocomposite owing to higher conjugation length than that of pure PANI. Thus,

FTIR study proves the successful formation of ANP nanocomposite by the well interaction of PANI, NF, and Ag nanoparticles without constructing any extra phase.

3.4 Electrical properties (DC)

Figure 5 depicts the room temperature conductivity of as-synthesized materials measured through the standard four-probe method. The conductivity of nanocomposites enhanced from 4.43 to 7.12 S/cm with an increase in silver particle concentration. The improvement in DC conductivity of nanocomposites is ascribed to the fine diffusion of silver nanoparticles in the polyaniline matrix during in situ polymerization, which is not possible in case of simple physical mixing. That, in turn, provides significant support and networking to electronic charge transportation in the polymer chain. Due to the formation of more efficient interconnected electrical pathways for charge transport in a polymer matrix with an increase in filler contents, there is a noticeable improvement in the conductivity of nanocomposites. This enhanced conductivity is significantly contributed in boost up of EMI shielding efficiency of synthesized materials.

3.5 Thermal properties

The thermogravimetric analysis is carried out in order to examine the thermal stability of PANI, $NiFe_2O_4$, and Ag/$NiFe_2O_4$/PANI nanocomposites as shown in Fig. 6. In the TGA graph, pure PANI has three major weight loss regions. The first region is observed around 110 °C due to the elimination of moisture contents. The second degradation process occurred nearby 220 °C, which is caused by the evaporation of dopants from the PANI chains [37]. Maximum weight loss noticed after 600 °C is attributed to the fully destruction of the polymer backbone chain. From TGA, it is worthy to note that nanocomposites have shown good thermal stability in comparison of pure PANI. The enhanced thermal
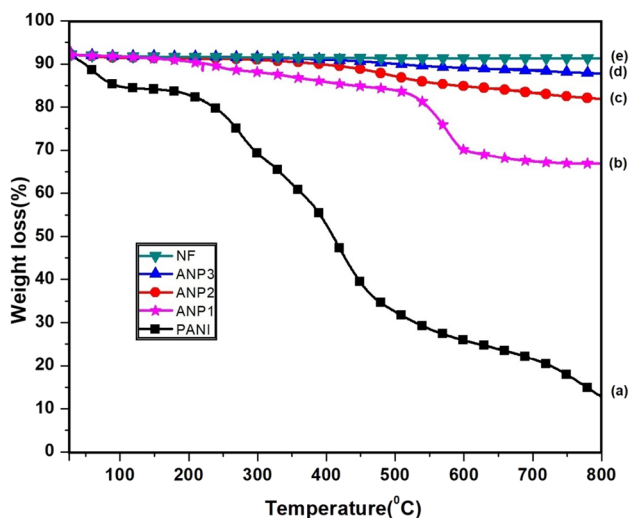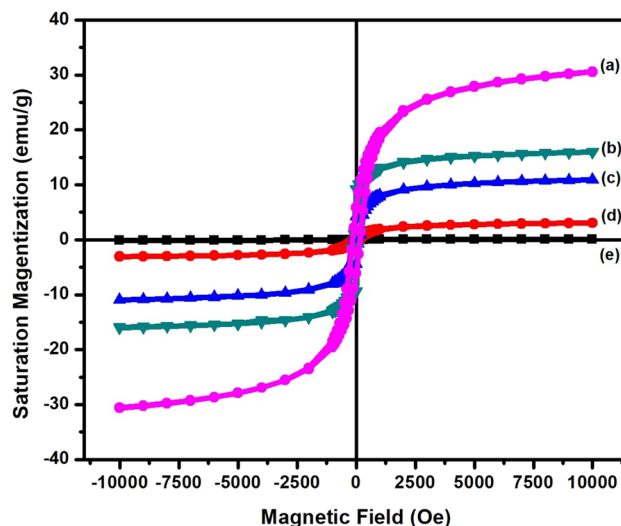

Fig. 7 Magnetic hysteresis loops of **a** NF, **b** ANP3, **c** ANP2, **d** ANP1, and **e** PANI

stability of fabricated compositions is ascribed to the well interaction of the NF and Ag nanoparticles with the PANI matrix [38], which creates hindrance in thermal movements of PANI chains in composite materials. Hence, synthesized composites can be useful for high-temperature applications.

3.6 Magnetic properties

Figure 7 depicts the M–H hysteretic curves of PANI, $NiFe_2O_4$,and Ag/$NiFe_2O_4$/PANI nanocomposites at room temperature. Pure $NiFe_2O_4$ material exhibits ferromagnetism with a magnetic saturation (M_S) value of 34.23 emug^{-1}. Although pure PANI exhibits the negligible magnetic behavior, ANP3, ANP2, and ANP1 nanocomposites showed improved M_S value of 10.98, 7.74, and 4.83 emug^{-1}, respectively, in VSM graph. When ferrite content are added in the polymer matrix, the M_S value of nanocomposites increases. However, these values are very less as compared to pure nickel ferrite because of the presence of two nonmagnetic silver and polymer materials in the nanocomposite, which results in decreasing interaction between the magnetic particles. According to the equation, $M_S = \varphi m_s$, magnetic

Fig. 6 Thermal curves of **a** PANI, **b** ANP1, **c** ANP2, **d** ANP3, and **e** NF

Table 2 Obtained magnetic parameters of NF and ANP1, ANP2, and ANP3 nanocomposites

Sample	Saturation magnetization (emug^{-1})	Coercivity (Oe)	Remanence magnetization (emug^{-1})
NF	35.65	220	13.26
ANP3	10.98	128	8.21
ANP2	7.74	91	6.39
ANP1	4.83	76	3.21

saturation primarily depends upon the volume fraction of the ferrite material particles (φ) and the saturation moment of the individual atom (m_s) [39]. Therefore, there is a decrease in the M_S value from 35.65 to 10.98 emug^{-1}. From VSM results (Table 2), it is clear that the Ag/NiF$_2$O$_4$/PANI nanocomposites exhibit ferromagnetic behavior. It also indicates the well dispersion of NF particles in the PANI matrix. The improved magnetic properties of nanocomposites can be beneficial for electromagnetic applications.

3.7 EMI shielding properties

When an electromagnetic (EM) radiation falls on some shielding material's surface, EMI shielding effectiveness (SE) of material is the contribution of three attenuation mechanisms, namely, reflection (SE$_R$), absorption (SE$_A$), or multiple reflections (SE$_M$) of the electromagnetic radiation. The overall EMI SE of a material can be represented by the following equation [40]:

$$SE_T(dB) = -10\log\left(\frac{P_T}{P_O}\right) = SE_R + SE_A + SE_M \tag{5}$$

where P_T is the transmitted power and P_o is the incident power of EM radiation, respectively. The multiple reflections can be ignored, if SE$_A \geq 10$ dB and SE$_R$ and SE$_A$ term can be depicted mathematically as [41]:

$$SE_R = -10\log(1 - R) \tag{6}$$

and

$$SE_A = -10\log\frac{T}{1 - R} \tag{7}$$

Figure 8 showcases the SE$_R$, SE$_A$, and SE$_T$ of synthesized materials as a function of X-band frequency. The total shielding effectiveness (SE$_T$) value of 21.98, 28.03, and 35.17 dB has been observed for ANP1, ANP2, and ANP3 samples, respectively. In the graphs (Fig. 8a, b), the SE$_A$ values of ANP nanocomposites found to be tremendously increasing as compared to SE$_R$. These results indicated that in ANP nanocomposites, the contribution towards overall shielding phenomena mostly comes from the absorption as compared to reflection. Moreover, ANP nanocomposites also exhibit excellent frequency stabilization in the applied frequency, which is found to be increased with increasing concentration of Ag nanoparticles. The SE values of nanocomposites enhanced with ferrite and silver filler concentration in the conducting matrix. Pure silver particles are non-magnetic in nature and contribute to absorption phenomena mainly due to its dielectric loss. Therefore, the Ag/NiFe$_2$O$_4$/PANI material composition possesses improved dielectric and magnetic losses in a broad frequency spectrum

as a result of interfacial polarization between polyaniline, NiFe$_2$O$_4$, and silver nanoparticles.

The addition of nickel ferrite and silver nanoparticles caused the higher magnetic and dielectric losses within synthesized nanocomposites. The shielding effectiveness (SE) also depends upon the complex permittivity and permeability of samples and can be written as [42]:

$$SE_A = 20\frac{d}{\delta}\log e = 20d\sqrt{\frac{\mu\omega\sigma}{2}}\cdot\log e \tag{8}$$

$$SE_R = 10\log\left(\frac{\sigma}{16\omega\mu\varepsilon}\right) \tag{9}$$

where 'd' is the thickness, ω is the angular frequency 'μ' is the magnetic permeability, 'ε' is free space permittivity, 'δ' is skin depth, and 'σ' is the conductivity of shielding material. From Eqs. 4 and 5, it can be noticed that there is increase in SE$_A$ values with the increase in frequency, while the SE$_R$ contribution decreases. As described above, SE$_A$ and SE$_R$ both depend upon the conductivity and permeability of the material. According to the free-electron theory, $\varepsilon'' = \sigma/\omega\varepsilon'$, the increased dielectric loss of silver particles is correlated to the electronic polarization process because of very high mobility of charge carriers. Also, the higher conductivity of silver nanoparticles has considerable contribution to skin effect. The skin effect was significantly decreased with the inclusion of silver particles within the polyaniline matrix. Hence, the coating of polyaniline on NiFe$_2$O$_4$ and silver materials provides improved impedance-matching characteristics that in turn enhanced the absorption properties of materials and showcased the superior shielding properties.

Figure 9I and II illustrates the real permittivity (ε') and imaginary permittivity (ε'') spectra of synthesized composites against frequency, calculated from the scattering parameters (S_{11}, S_{12}, S_{22}, and S_{21}) using the theory of Nicholson and Ross [43]. The real (ε') and imaginary parts (ε'') of permittivity are related to electric energy storage capability and dielectric loss capability, respectively, of the synthesized nanomaterials. From the permittivity graph, it is noticed that the 'ε''' and 'ε''' values of composites increase with the increase in the NF and Ag filler loadings.

Nanocomposites have shown the improved value up to 94.27 and 113.98 for ε' and ε'', respectively, with the doping of magnetic and silver materials. The permittivity performance of materials mainly depends on electronic, ionic, and space charge polarization. In this scenario, electric dipolar polarization becomes dominant over ionic or electronic polarization due to the heterogeneity of resulting products [44].

In a heterogeneous compound, the difference in ε', ε'' and conductivities at the interfaces of two medium results in
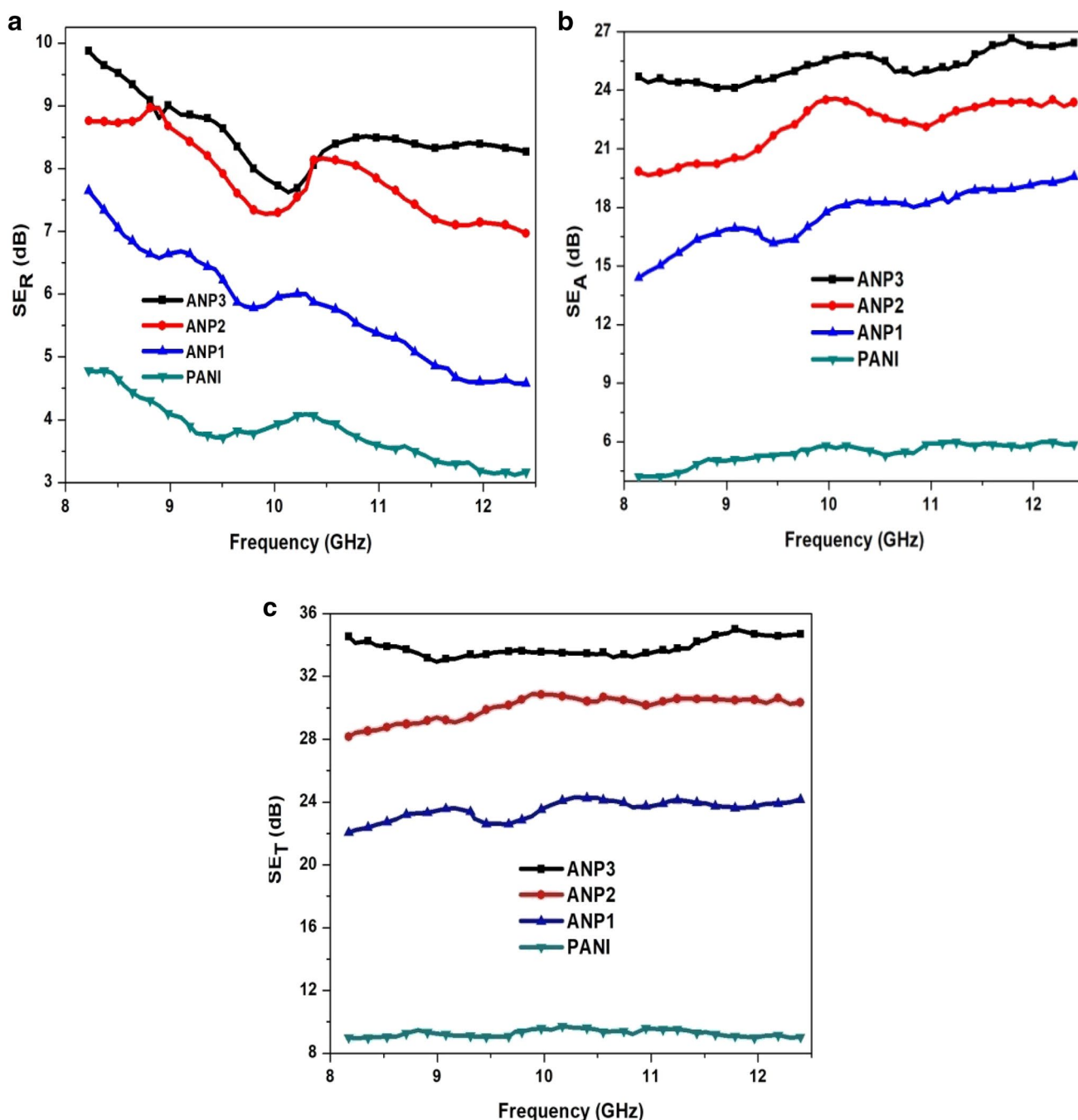
Fig. 8 **a–c** Variation of the SE_A, SE_R, and SE_T values of PANI, ANP1, ANP2, and ANP3 nanocomposites in X-band

interfacial polarization and is also called as Maxwell–Wagner polarization [45]. Herein, the inclusion of silver nanoparticles in the polyaniline matrix leads to different conductivity and permittivity values. Therefore, it shows interfacial polarization in the investigated frequency regime. The incorporation of insulating $NiFe_2O_4$ in the conducting matrix also results in enhanced interfacial area and heterogeneity of nanocomposites, which in turn offer improved absorption and shielding properties of the system.

Figure 9(III and IV) reveals the real (μ') and imaginary (μ'') part of permeability of synthesized materials, where μ' and μ'' signify the magnetic energy storage capability and magnetic loss capability, respectively, of the synthesized nanomaterials. The real part (μ') is found to be steady with the minute fluctuation in the measurements of fabricated samples, while the 'μ''' values of the composites are decreasing with the increasing frequency. The magnetic loss has been discovered significantly higher for high loadings of
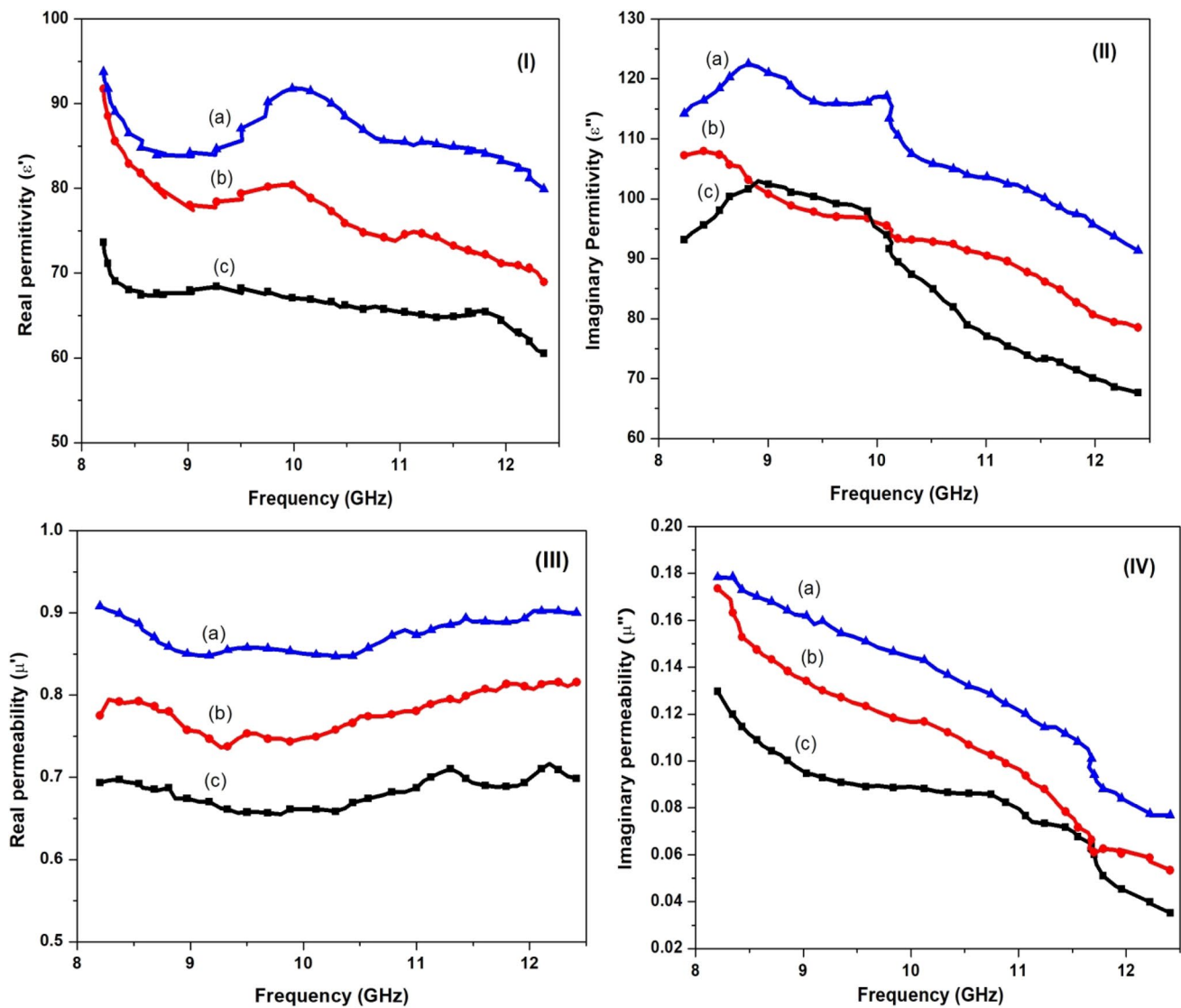
Fig. 9 **I, II** Complex permittivity and **III, IV** Complex permeability of Ag/NiFe$_2$O$_4$/PANI nanocomposites in X-band frequency

Table 3 Comparison of total SE of different polymer matrix with different fillers

Sample	Filler ratio	Frequency	Total SE	References
PANI/graphene sheet	25	8–12 GHz	34.2	[47]
Graphene/PMMA foam/graphene loading	1.8	8–12 GHz	13–19	[48]
MWNCT/Polyurethane	10	8.2–12.4	29	[49]
PANI/Fe$_3$O$_4$		12–18	11.5	[50]
MWCNT/polyurethane	25	8–12	25	[51]
PANI/fly ash	66.6	8.2–12.4, 12.4–18	32	[52]
PPy/PET fabric	–	0.05–1.5	36	[53]
MWCNT/MnZn ferrites/epoxy	4.0	7–12	17	[54]
PANI/Ag@graphene	5	0.4–1.6	29.33	[55]
Ag/NiFe$_2$O$_4$/PANI	0.75	8.2–12.4	35.17	Present work

NF content in the PANI matrix due to magnetic hysteresis attributes, natural resonance, and atomic domain wall expulsion of samples [46]. The observed dielectric and magnetic losses over the applied frequency improved the impedance-matching characteristics of synthesized composites, which in turn enhanced shielding properties due to synergistic effect of polyaniline, silver, and nickel ferrite nanoparticles.

In Table 3, there is a comparison of total shielding efficiency of various composite materials prepared from different types of fillers with different polymer matrix in varying frequency ranges. These results revealed that these ternary nanocomposites with effective shielding efficiency are prospective candidate as shielding material for various commercial EMI applications.

4 Conclusion

In summary, silver nanoparticle-decorated $NiFe_2O_4$/PANI nanocomposites were synthesized by in situ polymerization method. XRD, FTIR, and TEM analyses confirmed the construction of three-phase nanostructured composite materials. The synthesized compositions offer significantly enhanced conductivity and thermal and magnetic properties due to well dispersion of silver and ferrite particles in PANI matrix. The complex permittivity and permeability of investigated materials revealed the improved impedance matching and the effective complementarities between dielectric and magnetic loss of nanocomposites, which contributed to the superior EMI shielding performance. The nanocomposite with higher doping of fillers has achieved a maximum shielding effectiveness value of 35.17 dB in the X-band frequency. The obtained findings suggest that these nanocomposites have great potential to shield against electromagnetic radiation.

References

1. S. Gupta, C. Chang, C.-H. Lai, N.-H. Tai, Composites B **164**, 447–457 (2019)
2. M. Zahid, Y. Nawab, N. Gulzar, Z.A. Rehan, M.F. Shakir, A. Afzal, A. Rashid, A. Tariq, J. Mater. Sci.: Mater. Electron. **31**, 967–974 (2020)
3. J.-S. Li, H. Huang, Y.-J. Zhou, C.-Y. Zhang, Z.-T. Li, J. Mater. Res. 32, 1213 (2017)
4. A.K. Singh, A. Shishkin, T. Koppel, N. Gupta, Composites B **149**, 188 (2018)
5. N. Bagotia, V. Choudhary, D.K. Sharma, Composites B **159**, 378–388 (2019)
6. K. Reddy, H.M. Jeong, Y. Lee, A.V. Raghu, J. Polym. Sci. Part A **48**, 1477–1484 (2010)
7. M. Saini, R. Shukla, A. Kumar, J. Magn. Magn. Mater. **491**, 165549 (2019)
8. J.D. Sudha, S. Sivakala, R. Prasanth, V.L. Reena, P. Radhakrishnan Nair, Compos. Sci. Technol. **69**, 358 (2009)
9. H. Yoon, M. Chang, J. Jang, Adv. Funct. Mater. **17**, 431 (2007)
10. T. Yamauchi, S. Tansuriyavong, K. Doi, K. Oshima, M. Shimomura, N. Tsubokawa, S. Miyauchi, J.F.V. Vincent, Synth. Met. **152**, 45 (2005)
11. H. Gu, H. Zhang, J. Lin, Q. Shao, D.P. Young, L. Sun, T.D. Shen, Z. Guo, Polymer **143**, 324 (2018)
12. K. Gong, Q. Hu, Y. Xiao, X. Cheng, H. Liu, N. Wang, B. Qiu, Z. Guo, J. Mater. Chem. A **6**, 11119 (2018)
13. Y.-F. Zhu, L. Zhang, T. Natsuki, Y.-Q. Fu, Q.-Q. Ni, Synth. Met. **162**, 337 (2012)
14. H. Liu, A. Li, X. Ding, F. Yang, K. Sun, Solid State Sci. **93**, 7–12 (2019)
15. R. Valenzuela, Phys. Res. Int. **12**, 1–9 (2012)
16. K. Maaz, S. Karim, A. Mashiatullah, J. Liu, M.D. Hou, Y.M. Sun, J.L. Duan, H.J. Yao, D. Mo, Y.F. Chen, Phys B **404**, 3947 (2009)
17. N.N. Ali, Y. Atassi, A. Salloum, A. Charba, A. Malki, M. Jafarian, Mater. Chem. Phys. **211**, 79 (2018)
18. Q. Yue, C. Liu, Y. Wan, X. Wu, X. Zhang, P. Du, J. Catal. **358**, 1–7 (2018)
19. Ö. Yavuz, M.K. Ram, M. Aldissi, P. Poddar, S. Hariharan, J. Mater. Chem **15**, 810–817 (2005)
20. B.J. Madhu, M. Gurusiddesh, T. Kiran, B. Shruthi, H.S. Jayanna, J. Mater. Sci.: Mater. Electron. **27**, 7760 (2016)
21. C. Wang, Y. Shen, X. Wang, H. Zhang, A. Xie, Mater. Sci. Semicond. Process. **16**, 77–82 (2013)
22. J.C. Aphesteguy, P.G. Bercoff, S.E. Jacobo, Phys B **398**, 200–203 (2007)
23. Y. Wang, Y. Huang, Q. Wang, Q. He, L. Chen, Appl. Surf. Sci. **259**, 486–493 (2012)
24. J.P. Pouget, M.E. Jozefowicz, A.J. Epstein, X. Tang, A.G. MacDiarmid, Macromolecules **24**, 779–789 (1991)
25. M. Fu, Q. Jiao, Y. Zhao, J. Mater. Chem. A **1**, 5577 (2013)
26. S. Sagadevan, Z.Z. Chowdhury, R.F. Rafique, Mater. Res. **21**, 2 (2018)
27. M. Saini, S.K. Singh, R. Shukla, A. Kumar, J. Inorg. Organomet. Polym. Mater. **28**, 2306–2315 (2018)
28. R. Sharma, P. Thakur, M. Kumar, P.B. Barman, P. Sharma, V. Sharma, Ceram. Int. **43**, 13661–13669 (2017)
29. M.A. Hassan, M. Saqib, H. Shaikh, N.M. Ahmad, A. Elaissari, J. Biomed. Nanotechnol. **9**, 467–474 (2013)
30. Z.Z. Lazarevic, C. Jovalekic, A. Recnik, V.N. Ivanovski, A. Milutinovic, M. Romcevic et al., Mater. Res. Bull. **48**, 404–415 (2013)
31. G. Dixit, J.P. Singh, R.C. Srivastava, H.M. Agrawal, Nucl. Instrum. Methods B **269**, 133–139 (2011)
32. P. Sivakumar, R. Ramesh, A. Ramanand, S. Ponnusamy, C. Muthamizhchelvan, Mater. Res. Bull. **46**, 2204 (2011)
33. W. Feng, E. Sun, A. Fujii, H. Wu, K. Niihara, K. Yoshino, Bull. Chem. Soc. Jpn. **73**, 2627 (2000)
34. K. Gong, S. Guo, Y. Zhao, Q. Hu, H. Liu, D. Sun, M. Li, B. Qiu, Z. Guo, J. Mater. Chem. A **6**, 16824 (2018)
35. Ö. Yavuz, M.K. Ram, M. Aldissi, P. Poddar, S. Hariharan, J. Mater. Chem. **15**, 810 (2005)
36. M. Babazadeh, J. Appl. Polym. Sci. **113**, 3980 (2009)
37. P. Saini, V. Choudhary, B.P. Singh, R.B. Mathur, S.K. Dhawan, Mater. Chem. Phys. **113**, 919 (2009)
38. S. Sultana, M.Z. Khan, K. Umar, J. Alloys Compds. **535**, 44 (2012)
39. J. Jiang, L. Li, F. Xu, Mater. Sci. Eng. A **456**, 300–304 (2007)

40. W. Chen, J. Wang, B. Zhang, Q. Wu, X. Su, Mater. Res. Express **4**, 126303 (2017)
41. H.-B. Zhang, Q. Yan, W.-G. Zheng, Z. He, Z.-Z. Yu, ACS Appl. Mater. Interface **3**, 918 (2011)
42. A. Joshi, S. Datar, Pramana **84**, 1099 (2015)
43. A.M. Nicolson, G.F. Ross, IEEE Trans. Instrum. Means. **19**, 377–382 (1970)
44. M.A. Dar, K. Majid, M. Farukh, S.K. Dhawan, R.K. Kotnala, J. Shah, Arab. J. Chem. **12**, 5111–5119 (2016)
45. H.K. Choudhary, R. Kumar, S.P. Pawar, A.V. Anupama, S. Bose, B. Sahoo, Chem. Select **3**, 2120–2130 (2018)
46. A. Elahi, A. Shakoor, M. Irfan, N.A. Niaz, K. Mahmood, M.S. Awan, J. Mater. Sci.: Mater. Electron. **27**, 9489 (2016)
47. B. Yuan, L. Yu, L. Sheng, K. An, X. Zhao, J. Phys. D **45**, 235108 (2012)
48. H.B. Zhang, Q. Yan, W.G. Zheng, Z. He, Z.Z. Yu, A.C.S. Appl, Mater. Interfaces **3**, 918–924 (2011)
49. T.K. Gupta, B.P. Singh, S.R. Dhakate, V.N. Singh, R.B. Mathur, J. Mater. Chem. A **1**, 9138 (2013)
50. K. Singh, A. Ohlan, V.H. Pham, R. Balasubramaniyan, S. Varshney, J. Jang, S.H. Hur et al., Nanoscale **5**, 2411 (2013)
51. A.S. Hoang, Adv. Nat. Sci.: Nanosci. Nanotechnol. **2**, 025007 (2011)
52. A.P. Singh, A. Chandra, S. Dhawan, AIP Adv. **1**, 022147 (2011)
53. M.S. Kim, H.K. Kim, S.W. Byun, S.H. Jeong, Y.K. Hong, J.S. Joo, K.T. Song, J.K. Kim, C.J. Lee, J.Y. Lee, Synth. Met. **126**, 233–239 (2002)
54. C.H. Phan, M. Mariatti, Y.H. Koh, J. Magn. Magn. Mater. **401**, 472–478 (2016)
55. Y. Chen, Y. Li, M. Yip, N. Tai, Compos. Sci. Technol. **80**, 80–86 (2013)